The Astrophysical Journal, 613:95–108, 2004 September 20

WEAK-LENSING MASS DISTRIBUTIONS FOR 24 X-RAY ABELL CLUSTERS[1]

Eduardo S. Cypriano and Laerte Sodré, Jr.
Departamento de Astronomia, Instituto de Astronomia, Geofísica e Ciências Atmosféricas da Universidade de São Paolo, Rua do Matão, 1226, 05508-900 São Paulo, Brazil; eduardo@astro.iag.usp.br, laerte@astro.iag.usp.br

Jean-Paul Kneib
Observatoire Midi-Pyrénées, Laboratoire d'Astrophysique, UMR 5572, 14 Avenue E. Belin, 31400 Toulouse, France; and Astronomy Option, California Institute of Technology, MS 105-24, Pasadena, CA 91125; kneib@ast.obs-mip.fr, kneib@caltech.edu

and

Luis E. Campusano
Observatorio Astronómico Cerro Calán, Departamento de Astronomía, Universidad de Chile, Casilla 36-D, Santiago, Chile; luis@das.uchile.cl

Received 2003 September 30; accepted 2004 April 27

ABSTRACT

We use the weak gravitational lensing effect to study the mass distribution and dynamical state of a sample of 24 X-ray–luminous clusters of galaxies ($0.05 < z < 0.31$) observed with the FORS1 instrument mounted on the VLT-Antu (Unit Telescope 1) under homogeneous sky conditions and subarcsecond image quality. The galaxy shapes were measured in the combined *VIR* image after deconvolution with a locally determined point-spread function, while the two-dimensional mass distributions of the clusters were computed using an algorithm based on the maximum entropy method. By comparing the mass and light distributions of the clusters in our sample, we find that their centers of mass, for the majority of the clusters, are consistent with the positions of optical centers. We find that some clusters present significant mass substructures that generally have optical counterparts. In at least one cluster (A1451), we detect a mass substructure without an obvious luminous counterpart. The radial profile of the shear of the clusters was fitted using circular and elliptical isothermal distributions, which allowed the finding of a strong correlation between the orientation of the major axis of the matter distribution and the corresponding major axes of the brightest cluster galaxy light profiles. Estimates of how close to dynamical relaxation are these clusters were obtained through comparison of our weak-lensing mass measurements with the X-ray and velocity dispersion determinations available in the literature. We find that clusters with intracluster gas colder than 8 keV show good agreement between the different mass determinations, but clusters with gas hotter than 8 keV present weak-lensing masses smaller than those inferred by the other methods and therefore have been diagnosed to be out of equilibrium. These clusters are A1451, A2163, and A2744, all of which have hints of substructure. A2744 presents the largest discrepancy between its X-ray, velocity dispersion, and weak-lensing mass determinations, which can be interpreted as being due to the interaction between the two kinematic components along the line of sight found by Girardi & Mezzeti.

Subject headings: cosmology: observations — dark matter — galaxies: clusters: general — galaxies: clusters: individual (A2744, A1451, A2163) — gravitational lensing

Online material: extended figures

1. INTRODUCTION

The emergence of mass structures in the universe is currently linked to primordial density perturbations, dominated by cold dark matter, through a hierarchical clustering process involving gravitational instabilities. A natural consequence of this bottom-up scenario is that the most massive structures form later in time, and, depending on the world models, they are expected to show signatures of their assembling history. Since galaxy clusters are possibly the largest (nearly) virialized structures (e.g., Press & Schechter 1974), the study of their main properties (e.g., masses, shapes, radial profiles) can provide valuable clues about the details of the agglomeration of matter in the universe and hence on the nature of the dark matter (e.g., Kauffmann et al. 1999). Clusters can also be used as cosmological probes providing additional data that, together with cosmic microwave background observations, can be used in the determination of several cosmological parameters. Studies of their mass function (e.g., Henry & Arnaud 1991; Reiprich & Böhringer 2002), mass-to-light ratio (e.g., Bahcall et al. 1995; Carlberg et al. 1996), and baryon fraction (e.g., White & Frenk 1991; Allen et al. 2002) can provide constraints on key cosmological parameters like the mass density parameter, Ω_M, and the bias, and on the power-spectrum amplitude and shape parameter (Lacey & Cole 1994; Bahcall & Fan 1998).

Galaxy clusters are complex systems that hold together galaxies, hot gas, and dark matter. These components are governed by different physical mechanisms, and their study requires the use of different observational techniques. Imaging in visible light reveals clusters through their member galaxies, which we know now contribute only a small fraction of the cluster total mass. But if these galaxies are in virial equilibrium, the depth of the cluster potential well can be accessed through their velocity

[1] Based on observations collected with ESO Very Large Telescope–Antu (UT1).

dispersion, although the continuous accretion of field galaxies can bias the mass measurements to higher values (e.g., Sodré et al. 1989). The thin hot gas—mainly hydrogen—that permeates the cluster gravitational potential is found to be at temperatures of the order of 10^7–10^8 K, and thus is fully ionized and emitting X-rays via the thermal bremsstrahlung process (see Sarazin 1988 for a more complete discussion). The emission in the X-ray band provides an efficient method to find galaxy clusters and estimates of the cluster masses if the hypothesis that the gas is in hydrodynamic equilibrium is adopted. The advantage of using the hot intracluster gas rather than the member galaxies for mass determinations is that it has a much shorter relaxation time as a result of its self-interactivity (Sarazin 1988). Nevertheless, there is evidence that many clusters present significant departures from dynamical relaxation (e.g., Geller & Beers 1982; Sodré et al. 2001). Presumably, the clusters that are at the top of the mass function will achieve their formation process last, so we expect to find some degree of correlation between the departures from equilibrium and the mass of the clusters.

The development of gravitational lensing techniques, for both the strong and weak regimes, has presented a new way of measuring masses, regardless of the nature or dynamical state of the matter (Fort & Mellier 1994; Mellier 1999). Strong lensing, which relies on the modeling of systems of multiple lensed background galaxies, has proved to be an accurate method, mainly when the number of gravitational arcs is large (e.g., Kneib et al. 1996). However, this technique can probe only the very central regions of the clusters and is limited to the most massive and concentrated objects. On the other hand, the statistical analysis of the weak distortion caused by the cluster shear field on images of faint background galaxies allows the mapping of the matter distribution to much larger radius; besides, this gravitational distortion is detectable in almost all clusters when large telescopes with current instrumentation are used. After the seminal work of Tyson et al. (1990), the weak-lensing technique started to be used for the study of some clusters having special interest because of extreme values in some of their measured properties, and new methodologies were established (see Mellier 1999 for a review).

With the development of wide-field cameras and the increase in the number of large telescopes, it is now possible to study large samples of galaxy clusters selected using well-defined criteria, ideally observed under similar conditions and analyzed with the same technique. Dahle et al. (2002) studied 38 northern X-ray luminous clusters using data collected with 2 m class telescopes and selected to be representative of the most massive clusters in the $0.15 < z < 0.35$ redshift range. However, the clusters in this sample were not all observed with the same instruments and sometimes were observed under varying atmospheric conditions.

In this paper we present a weak-lensing analysis of a sample of 24 X-ray luminous southern clusters with $0.05 < z < 0.31$, based on imaging observations with the ESO-VLT telescope taken under subarcsecond conditions. The clusters were selected from the X-Ray Bright Abell Cluster Survey (XBACS; Ebeling et al. 1996), with $-50^\circ < \delta < 15^\circ$, $12^{\rm h} \leq \alpha < 1^{\rm h}$ (J2000.0), and $L_{\rm X} > 5 \times 10^{44}$ ergs s^{-1}. Similar observations have been done of a complementary sample of 27 X-ray clusters, with $1^{\rm h} \leq \alpha < 12^{\rm h}$, whose weak-lensing analysis is underway. Hereafter, and because of the rather rare choice of a lower z limit of 0.05, we refer to our whole VLT survey as the Low-z Lensing Survey of X-Ray Luminous Clusters (LZLS), and the sample presented here is its part I. The data used in this paper derive from observations primarily designed for detection of strong-lensing features but conceived for weak-lensing measurements also; the service observing mode at ESO was essential to ensure the high quality and homogeneity of the images. The statistics of the occurrence of bright arcs for the whole LZLS survey will be presented in a separate paper (L. Campusano et al. 2004, in preparation), together with its implications with respect to the clusters' inner mass radial profiles. In future papers, we will address the combined evaluation of the mass distribution and we will use both weak and strong lensing in those LZLS clusters with gravitational arcs.

In this paper we determine the mass distributions for the galaxy clusters in our sample and their total masses using weak-lensing techniques and investigate their dynamical state through comparison of the weak-lensing masses with already published virial and X-ray mass estimates. In § 2 we describe the sample selection and the observations. In § 3 we present the procedures adopted in the weak-lensing analysis, including galaxy shape measurements and the reconstruction of cluster density maps, as well as the results obtained. The discussion of the results is presented in § 4, together with the comparison with dynamical, X-ray and weak-lensing masses taken from the literature. In § 5 we summarize our main conclusions. In Figure 8 in the Appendix, we display images, mass and light maps, and weak-shear profiles for the cluster sample.

Throughout this paper we adopt $\Omega_M = 0.3$, $\Omega_\Lambda = 0.7$, and $H_0 = 70$ km s^{-1} Mpc^{-1}.

2. OBSERVATIONS

2.1. *Sample Selection*

The galaxy clusters investigated in this work were selected on the basis of their high X-ray luminosities ($L_{\rm X}$). Initially, we selected clusters in the X-Ray Brightest Abell Cluster Catalog (XBAC; Ebeling et al. 1996) with $L_{\rm X} \geq 5 \times 10^{44}$ ergs s^{-1} in the 0.1–2.4 keV band, which constitutes a good threshold to identify real, massive clusters (e.g., Luppino et al. 1999). We then restricted the sample to clusters that could be reached with ESO VLT ($-50^\circ \leq \delta < +15^\circ$). A low-$z$ limit of 0.05 was chosen, because for lower redshifts the angular size of the clusters is too large compared with the field of the imaging camera. For $z < 0.05$, possible gravitational arcs would appear projected deep inside the central galaxy image and the angular size of cluster galaxies in the camera field would be very high, making it hard to find a suitable number of background galaxies (without strong light contamination) for a weak-lensing analysis. ESO VLT was considered a very good choice because the observations could be completed with some 10 hr of service observing and the homogeneity and image quality of the observations could be optimally achieved. These criteria produced 27 targets within $12^{\rm h} \leq \alpha < 1^{\rm h}$. Three of these clusters (A68, A1689, and A1835) have been already observed with the *Hubble Space Telescope* (*HST*) and the Canada-France-Hawaii Telescope (CFHT) by one of us (J. P. K.), and the results are published elsewhere (Smith et al. 2003; S. Bardeau et al. 2004, in preparation). The remaining 24 rich galaxy clusters that are studied in this paper are presented in Table 1. This sample constitutes part I of the VLT LZLS.

2.2. *Imaging and Data Reduction*

All clusters were observed in service mode using VLT-Antu (Unit Telescope 1), from 2001 April to July (ESO program 67.A-0597), with the FORS1 instrument (Focal Reducer/Low-Dispersion Spectrograph) working in its imaging mode.

TABLE 1
VLT Low-z Lensing Survey of X-Ray–Luminous Clusters (LZLS): Part I

Cluster Name (1)	R.A. (2)	Decl. (3)	z (4)	L_X (10^{44} ergs s^{-1}) (5)	seeing (arcsec) (6)	μ_{sky} (1 σ) (R mag arcsec^{-2}) (7)
A2744[a]	00 14 16.1	−30 22 58.8	0.308	22.05	0.59	26.92
A22	00 20 38.6	−25 43 19.2	0.141	5.31	0.60	26.71
A85	00 41 48.7	−09 19 04.8	0.056	8.38	0.59	26.58
A2811	00 42 07.9	−28 32 09.6	0.108	5.43	0.64	26.77
A1437	12 00 25.4	03 21 03.6	0.134	7.72	0.52	26.22
A1451	12 03 14.6	−21 31 37.2	0.199	7.40	0.48	26.37
A1553	12 30 48.0	10 33 21.6	0.165	7.05	0.80	26.10
A1650	12 58 41.8	−01 45 21.6	0.084	7.81	0.68	26.28
A1651	12 59 24.0	−04 11 20.4	0.085	8.25	0.76	26.31
A1664	13 03 44.2	−24 15 21.6	0.128	5.36	0.79	26.51
A2029	15 10 55.0	05 43 12.0	0.077	15.35	0.42	26.21
A2104	15 40 06.5	−03 18 21.6	0.155	7.89	0.41	26.30
A2163	16 15 49.4	−06 09 00.0	0.208	37.50	0.43	26.43
A2204	16 32 46.8	05 34 26.4	0.152	20.58	0.49	26.25
A3695	20 34 46.6	−35 49 48.0	0.089	5.07	0.76	26.63
A3739	21 04 17.5	−41 20 20.4	0.166	7.00	0.70	26.66
A2345	21 26 58.6	−12 08 27.6	0.176	9.93	0.56	26.37
A2384	21 52 16.6	−19 36 00.0	0.094	6.82	0.61	26.28
A2426	22 14 32.4	−10 21 54.0	0.099	5.10	0.81	26.64
A3856	22 18 37.4	−38 53 13.2	0.142	6.40	0.77	26.85
A3888	22 34 32.9	−37 43 58.8	0.151	14.52	1.03	26.75
A3984	23 15 37.7	−37 44 52.8	0.178	9.18	0.53	26.92
A2597	23 25 16.6	−12 07 26.4	0.085	7.97	0.52	26.64
A4010	23 31 14.2	−36 30 07.2	0.096	5.55	0.55	26.92

Notes.—Col. (1): Cluster name. Cols. (2) and (3): Equatorial J2000.0 coordinates. Units of right ascension are hours, minutes, and seconds, and units of declination are degrees, arcminutes, and arcseconds. Col. (4): Redshift (H. Andernach & E. Tago 2004, in preparation). Col. (5): X-ray luminosities in the 0.1–2.4 keV band (Ebeling et al. 1996). Col. (6): FWHM of stellar images in the combined *VRI* image. Col. (7): Surface brightness corresponding to 1 σ above the sky average in the R image.
[a] A2744 is also known as AC 118.

FORS1 employs a TK2048EB4-1 back-illuminated thinned CCD with 2048×2048 pixels, each with 24×24 μm^2 area. The employed imaging mode of FORS1 results in a pixel scale of 0.″2 and a square field of view of 6.′8 on a side, corresponding to 0.4, 0.9, and 1.8 Mpc at the smaller, median, and greater redshifts of the clusters of our sample, which are 0.05, 0.126, and 0.305, respectively. The imaging was chosen to be centered on the cluster cores and done through the V, R, and I bands with exposure times of 330 s in each filter, ensuring a good detection of faint galaxies in all bands. The color information is essential for discriminating elongated objects belonging to the cluster from the background sources needed for the weak-lensing measurements. All observations were conducted under good sky transparency and had an excellent image quality characterized by seeing ranging from 0.″4 to 1.″0, with a median seeing of 0.″6.

The data were reduced in a standard way using IRAF packages. For each cluster we combined the images in the three filters, normalizing by their modes, to produce a high signal-to-noise *VRI* image that was used for the weak-lensing analysis. The images in each band were used for the photometry of the objects in each cluster field. Comparing stellar shapes measured in the *VRI* images with those from the single-band ones, we concluded that the combination process did not introduce biases. Tests on galaxies revealed that the use of the combined *VRI* image improves the precision in the shape measurements over single-band measurements.

Zero-point magnitudes, extinction, and color coefficients for transformations from instrumental to standard magnitudes were provided by the ESO pipeline. Almost all data were collected under photometric sky conditions or nearly so. Table 1 contains, in addition to general information about each cluster in our sample, the seeing (FWHM) derived from stellar images in the combined *VRI* image. The table also includes the surface brightness corresponding to a 1 σ fluctuation above the sky background in the R image, which is a measure of the quality and depth of these images.

3. WEAK-LENSING ANALYSIS

3.1. *Construction of the Catalog*

The detection of objects in the images and the extraction of their main parameters were made with SExtractor (Bertin & Arnouts 1996). We ran this program separately for the single-band images and for the combined one. The four catalogs obtained were then combined by matching the Cartesian position of the objects, with a tolerance of 0.″6.

Magnitudes (SExtractor's *mag_best*) were measured in the single-band images, and the colors were computed using 4″ diameter apertures. Astrometric and morphological data were obtained from the *VRI* image.

We have produced three subsamples of detected objects: stars, cluster galaxies, and other galaxies. Stars have been selected using two different criteria. For unsaturated objects ($R \gtrsim 20.0$ mag) we have used the FWHM of their light profiles. In Figure 1 we show an example of the distribution of this parameter as a function of R magnitude, which shows that stars

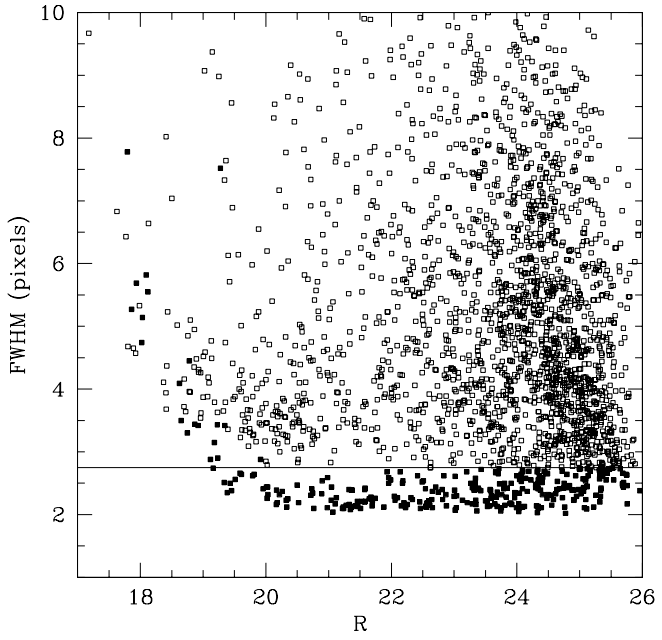

FIG. 1.—Magnitude-FWHM diagram for objects in the field of A1451. Filled squares represent objects classified as pointlike sources, following the criteria described in the text. The continuous line is the threshold FWHM adopted for star/galaxy separation of objects fainter than $R = 20$. The star sequence for unsaturated objects is clearly identifiable below the line.

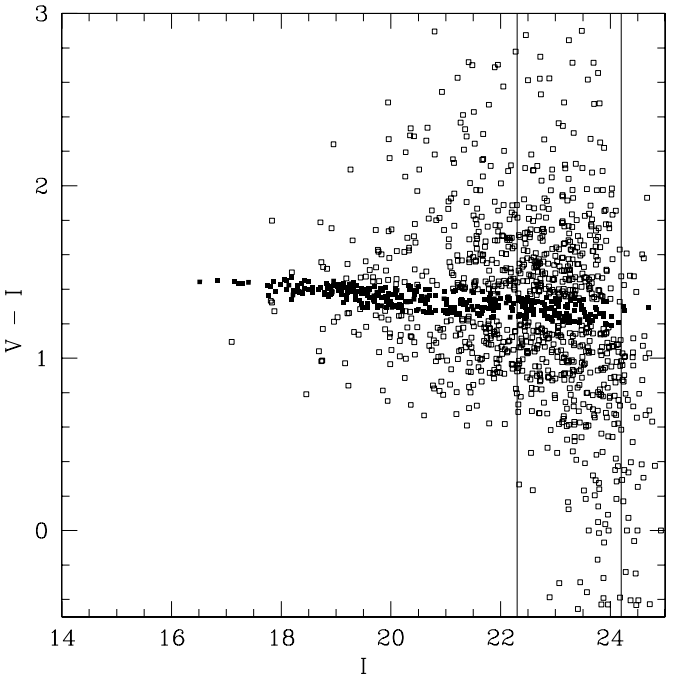

FIG. 2.—Color-magnitude diagram for galaxies in the field of A1451. Galaxies belonging to the red cluster sequence are shown as filled squares. The vertical lines show the range of magnitude for the galaxies used for the lensing analysis.

can be easily separated from galaxies down to very faint magnitudes. For brighter objects, we have used the SExtractor neural network classifier.

In the absence of spectroscopic redshifts for most of the galaxies in the clusters, the cluster galaxies were selected from the color-magnitude diagram of $(V - I)$ versus I for each cluster (Fig. 2). In this type of diagram, the early-type cluster galaxies occupy a well defined locus, the so-called red cluster sequence, with almost the same color. After determining the typical color of the ellipticals in each cluster, we selected as cluster galaxies those with colors within a strip of width 0.2 mag matching the cluster red sequence. This selection procedure naturally will not include the bluer galaxies belonging to a particular cluster and having colors outside the color range defined by the strip in the cluster color-magnitude diagram. These bluer galaxies not recognized as cluster members cannot be distinguished from the background galaxies needed for the weak-lensing analysis and thus may introduce a certain level of "noise." We return to this issue below.

3.2. *Shape Measurements*

Weak-lensing analysis needs careful measurements of the ellipticity of background galaxies observed in the field of a cluster of galaxies.

We made galaxy shape measurements, including the correction of the seeing circularization and point-spread function (PSF) anisotropies, using the IM2SHAPE software (Bridle et al. 2002). Following a proposition by Kuijken (1999), this software models astronomical objects with a sum of Gaussians with elliptical base. Let $\boldsymbol{x}$ be a position on a CCD image. The intensity of a galaxy as a function of position is modeled as

$$I(\boldsymbol{x}) = \sum_i \frac{A_i}{2\pi|C_i|} e^{-(\boldsymbol{x}-\boldsymbol{x}_i)^T C_i (\boldsymbol{x}-\boldsymbol{x}_i)/2}, \quad (1)$$

where the $\boldsymbol{x}_i$, A_i, and C_i are, respectively, the center of each Gaussian, its amplitude, and its covariance matrix. The components of C_i can be written in terms of the ellipse parameters a, b, and θ, which are its semimajor and semiminor axes and the position angle of the major axis, respectively. The ellipticity, following the convention usually adopted in lensing studies, is defined as

$$\epsilon = \frac{a - b}{a + b}. \quad (2)$$

At this point it is convenient to define the ellipticity projected tangentially to the direction of a predefined cluster center of mass,

$$\epsilon_t = \epsilon \cos[2(\theta - \phi)], \quad (3)$$

where ϕ is the azimuthal coordinate of the galaxy.

IM2SHAPE uses a Bayesian approach to determine these parameters, with carefully calculated uncertainty estimates. It also deconvolves the measured shape using a PSF that is also given as a sum of Gaussians, so that the deconvolution process can then be done in a fully analytical way.

The steps actually performed in measuring galaxy shapes on our images can be summarized as follows. First, IM2SHAPE is used to model images of the unsaturated stellar objects as single Gaussians. These stars (in fact, stellar-like objects) are divided into four sets, following their positions in the CCD quadrants. Stars with ϵ, θ, or base area unrepresentative of their respective quadrant averages are removed through a 2 σ clipping process. This cleaned star catalog is used to map the PSF along the field. After that, the same program is applied to the galaxies in the CCD image. Each galaxy image is modeled as a sum of two Gaussians, which is adequate for exponential and de Vaucouleurs profiles, given typical galaxy sizes, CCD pixel sizes, and PSFs (see Kuijken 1999 for a discussion). The parameters x, y, ϵ, and θ are forced to be the same for both Gaussians. Using the five nearest stars, a local PSF is calculated for the position of each

galaxy, and a deconvolution of their images is performed. The result of this procedure is a list with the elliptical parameters of the galaxies in a cluster field.

3.3. *Weak-Lensing Sample Selection*

A key step in weak-lensing analysis is the selection of galaxies that will be used as probes of the gravitational field of the lensing cluster. These galaxies must be behind the cluster, and we should be able to measure their shapes with good accuracy. For this, it is necessary to have distance estimates for all objects in the field. It is possible to select background galaxies through photometric redshifts (e.g., Athreya et al. 2002), but an efficient application of this technique requires more abundant color information than what we have. In the absence of redshift information, we proceeded by building a master catalog of putative background galaxies, selected by flux in the noncluster galaxy catalog. We selected only galaxies with absolute R-band magnitude fainter than -16.6 at the cluster distance (roughly $M^* + 5$; Goto et al. 2002). This magnitude cutoff was chosen as a compromise solution that minimized the foreground/cluster contamination while leaving a reasonable number of galaxies in the weak-lensing sample.

The final catalog is obtained after removal of a number of objects obeying the following criteria. Initially, all objects inside a radius of $1'$ around the cluster center were excluded from the lensing sample (following, e.g., Hoekstra et al. 2002). The reason for this is twofold. First, in these regions (mainly the inner $30''$) mass densities are closer to the critical value, and then the weak-lensing regime is no longer a good approximation. Second, in central regions there is a high surface density of low luminosity cluster components and diffuse light, which can contaminate the weak-lensing sample and bias the shape measurements.

Relevant cases of light contamination by luminous neighbors were detected by comparing differences in the object center estimated by SExtractor and IM2SHAPE, because the first has a deblending procedure, while the second does not. Thus, objects with differences between center estimates greater than 3 pixels were also removed from the sample. Finally, all galaxies with uncertainties in ϵ_t larger than 0.35 were also removed. We found that this value is a good compromise between the total number of galaxies in the final sample and the accuracy of shape measurements. It should be stressed, however, that the results presented here depend only weakly on this value, since in the whole analysis the inverse-squares of the uncertainties are used as statistical weights (see, e.g., § 3.5).

The total number of galaxies in each cluster field useful for shear measurements is presented in column (2) of Table 2. Their surface density ranges from 4.7 to 17.8 galaxies arcmin^{-2}. This broad range is due to almost unavoidable differences in the deepness of the images (see the values of the seeing and $\mu_{\rm sky}$ in Table 1) and also to the different bright apparent-magnitude cutoffs for the galaxy lensing samples.

3.4. *Mass and Light Maps*

In the weak-lensing regime, the mass distribution can be obtained from the pattern of distortion of galaxy shapes at a position $\boldsymbol{x}$, $\langle \epsilon_t(\boldsymbol{x}) \rangle$, that depends only on the reduced shear $g = \gamma/(1-\kappa)$, where γ and κ are the shear modulus and convergence at $\boldsymbol{x}$. The latter is proportional to the mass density and is defined as

$$\kappa = \frac{\sum(\boldsymbol{x})}{\sum_c}, \tag{4}$$

where the critical surface density Σ_c is given by

$$\sum\nolimits_c = \frac{c^2}{4\pi G}\frac{D_s}{D_l D_{ls}} \tag{5}$$

and D_l, D_s, and D_{ls} are the angular diameter distances from the observer to the lens, from the observer to the source, and from the lens to the source, respectively.

We have reconstructed the two-dimensional mass density distributions from distortion maps using the LENSENT software (Bridle et al. 1998; Marshall et al. 2002). This software computes κ maps using a maximum entropy method, taking each background galaxy image shape as an independent estimator of the reduced shear field. This map is smoothed by a Gaussian function, called the intrinsic correlation function (ICF), whose FWHM is determined by Bayesian methods. The program avoids any binning of the data and allows the reconstruction of complex mass distributions. We present in column (3) of Table 2 the optimal ICF-FWHM for the smoothing function found by LENSENT.

The resultant mass maps for all clusters, with 64×64 pixels across, can be seen in the Appendix. In order to minimize edge effects, LENSENT produces maps in a grid twice as big as the data region. Here we only show the part of a map corresponding to the field actually observed.

It should be noted that since this method takes into account only galaxy distortions and ignores their amplifications, the convergence determined this way will suffer from the "mass sheet degeneracy": the distortion pattern can be reproduced by any mass distributions that obeys the transformation $\kappa \rightarrow \lambda\kappa + (1-\lambda)$, where λ is a real number.

To estimate the significance of the features found in mass maps we have also performed 100 bootstrap realizations for each cluster, adding Gaussian noise to galaxy ellipticities, with amplitude equal to their observational errors. From the mass maps produced in the simulations, we computed a standard deviation (σ) map, and by dividing the mass map by the σ-map, we obtained a significance map. The significance maps show that most clusters present individual pixel signal-to-noise ratios ranging between 1 and 3, with values as high as 8 found in some cases.

We have also computed light maps (also shown in the Appendix) of the light distribution of galaxies in the red sequence. The field is divided into 32×32 pixels, and the smoothed light density of each pixel is estimated as

$$\mathcal{L} \propto \sum_i L_i e^{-d_i^2/2\sigma^2}, \tag{6}$$

where L_i is the luminosity of the ith galaxy and d_i is its angular distance to the pixel center. The value of σ is chosen to have the same FWHM as the ICF of the mass map. See in Figure 3 an example of mass and light maps.

For two clusters, A1651 and A1664, the algorithm was not able to reconstruct the density distribution. This is discussed in § 4.6.

3.5. *Profile Fitting*

In order to avoid the mass sheet degeneracy and to obtain quantities that can be compared with data determined by other methods, we fitted physically motivated parametric models to the distortion maps. We considered two different mass models: a singular isothermal sphere (SIS) and a singular isothermal ellipsoid (SIE).

Let us assume a polar reference system with origin at the cluster center, so that any point on the image can be represented

TABLE 2

BEST-FIT PARAMETERS

				SIS			SIE				PL		
CLUSTER NAME	NUMBER	ICF-FWHM	$\langle z \rangle$	θ_E	σ_{SIS}	χ^2_{red}	σ_{SIE}	f	α	χ^2_{red}	θ_E	q	χ^2_{red}
(1)	(2)	(3)	(4)	(5)	(6)	(7)	(8)	(9)	(10)	(11)	(12)	(13)	(14)
A2744	323	220	1.01 ± 0.04	28 ± 4	1491 ± 116	1.54	1545 ± 111	0.5 ± 0.2	2 ± 17	1.53	6 ± 14	0.02	1.51
A22	517	240	0.87 ± 0.04	10 ± 4	718 ± 132	1.50	887 ± 92	...	15 ± 12	1.49	24 ± 5	1.98	1.50
A85	492	110	0.81 ± 0.05	21 ± 4	917 ± 85	1.11	926 ± 82	0.5 ± 0.3	21 ± 22	1.11	20 ± 5	0.96	1.11
A2811	498	80	0.86 ± 0.05	16 ± 6	863 ± 149	1.13	891 ± 134	...	−35 ± 15	1.13	1 ± 4	0.16	1.13
A1437	385	160	0.84 ± 0.05	11 ± 4	734 ± 152	0.95	780 ± 127	...	46 ± 17	0.94	13 ± 6	1.14	0.95
A1451	418	80	0.90 ± 0.05	17 ± 4	993 ± 114	0.98	1087 ± 98	...	−15 ± 10	0.94	24 ± 4	1.47	0.98
A1553	178	160	0.81 ± 0.05	15 ± 6	923 ± 186	1.05	925 ± 164	...	−49 ± 20	1.05	1 ± 9	0.10	1.05
A1650	279	160	0.80 ± 0.05	18 ± 5	876 ± 133	1.08	1033 ± 109	...	−29 ± 11	1.06	1 ± 6	0.04	1.08
A1651	391	...	0.73 ± 0.04	1 ± 5	210 ± 498	0.91	489 ± 116	...	71 ± 48	0.91	13 ± 10	2.00	0.91
A1664	246	...	0.80 ± 0.05	−2 ± 6	...	...	402 ± 264	...	−74 ± 93	1.05	...	...	...
A2029	549	140	0.83 ± 0.05	25 ± 3	1039 ± 64	0.86	1052 ± 63	0.6 ± 0.2	−26 ± 20	0.86	13 ± 6	0.40	0.86
A2104	378	90	0.86 ± 0.05	21 ± 4	1039 ± 108	0.86	1038 ± 102	0.4 ± 0.2	58 ± 14	0.86	20 ± 6	0.96	0.86
A2163	261	240	0.89 ± 0.04	18 ± 5	1021 ± 146	0.90	1094 ± 125	...	−84 ± 12	0.89	27 ± 7	1.60	0.90
A2204	347	110	0.86 ± 0.05	20 ± 4	1028 ± 104	0.81	1035 ± 102	0.6 ± 0.3	10 ± 28	0.81	19 ± 5	0.92	0.81
A3695	294	130	0.83 ± 0.05	20 ± 5	928 ± 117	1.10	987 ± 104	...	−23 ± 11	1.09	7 ± 9	0.38	1.10
A3739	246	110	0.88 ± 0.04	23 ± 5	1187 ± 107	1.05	1194 ± 92	...	32 ± 7	1.05	3 ± 13	0.02	0.98
A2345	364	150	0.89 ± 0.05	15 ± 5	909 ± 138	1.08	965 ± 126	...	87 ± 14	1.08	1 ± 6	0.10	1.08
A2384	420	150	0.80 ± 0.05	12 ± 4	737 ± 126	1.05	787 ± 108	...	19 ± 14	1.05	2 ± 5	0.32	1.05
A2426	342	210	0.80 ± 0.05	10 ± 5	676 ± 158	0.91	767 ± 132	...	59 ± 18	0.90	1 ± 4	0.24	0.90
A3856	423	110	0.87 ± 0.05	20 ± 4	1001 ± 100	1.05	1022 ± 93	...	−33 ± 9	1.03	22 ± 5	1.10	1.05
A3888	270	130	0.86 ± 0.05	19 ± 5	981 ± 125	1.21	1008 ± 125	0.6 ± 0.4	79 ± 34	1.22	1 ± 9	0.02	1.20
A3984	607	210	0.95 ± 0.05	22 ± 3	1093 ± 77	1.27	1150 ± 66	...	55 ± 6	1.25	3 ± 7	0.08	1.26
A2597	524	150	0.89 ± 0.04	14 ± 4	776 ± 101	1.03	853 ± 79	...	−19 ± 11	1.01	1 ± 4	0.14	1.03
A4010	673	160	0.87 ± 0.04	11 ± 3	706 ± 104	1.27	776 ± 84	...	57 ± 12	1.26	9 ± 4	0.86	1.27

NOTES.—Col. (1): Cluster name. Col. (2): Number of galaxies used for weak-lensing analysis. Col. (3): FWHM of the smoothing function used to build the mass map in arcsec. Col. (4): Average redshift and standard deviation of the galaxies in the weak-lensing sample (see text for details). Cols. (5) and (6): The Einstein radius (in arcsec) and σ_{SIS} and the respective uncertainties obtained by the fitting of an SIS profile. Col. (7): The χ^2_{red} of the SIS fit divided by the number of degrees of freedom. Cols. (8), (9), and (10): σ_{SIE}, axial ratio, and position angle (measured from north to east) and respective uncertainties obtained by the fitting of an SIE profile. When the best SIE fit gives a value of f smaller than 0.3, we have done the fit again using a fixed value of $f = 0.3$ and left the entry for f in the table empty. Col. (11): The χ^2_{red} of the SIE fit divided by the number of degrees of freedom. Cols. (12), (13), and (14): The Einstein radius, the slope of the two-dimensional density profile, and the χ^2_{red} given by the fitting of a power law profile. The errors on q were omitted because they are too small, ranging from 0.0008 to 0.0117.

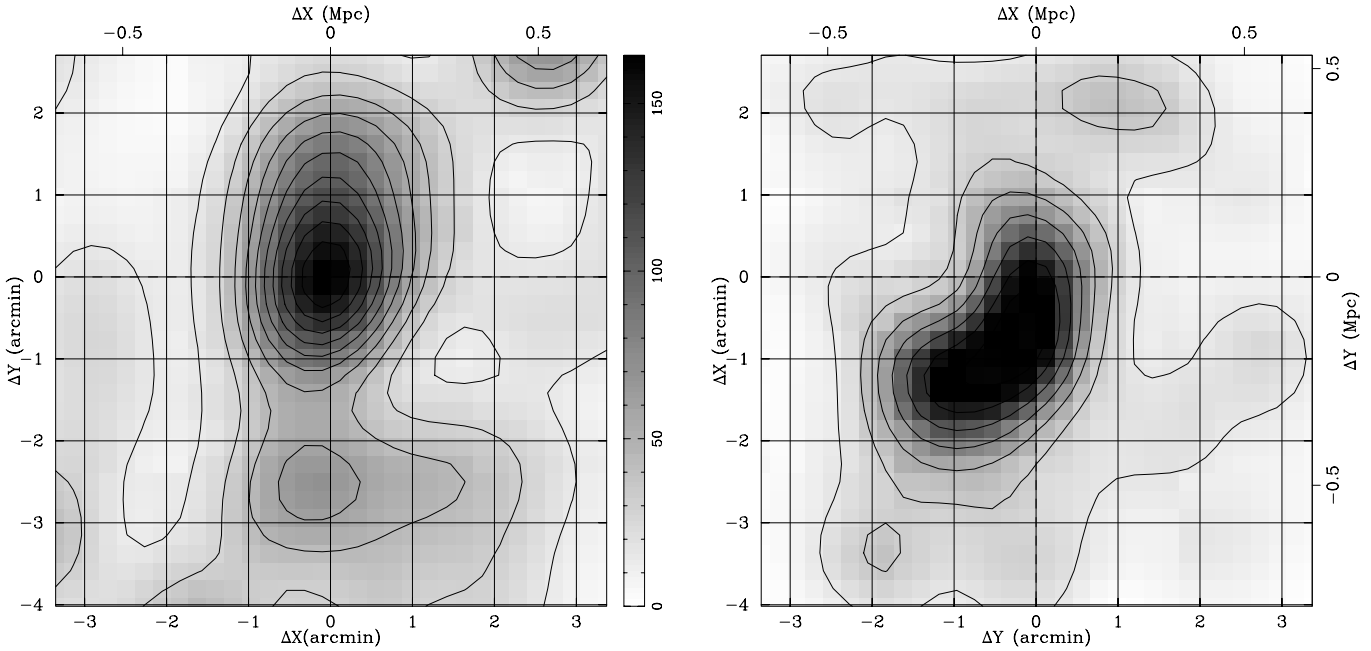

FIG. 3.—Mass (*left*) and light (*right*) maps for the cluster A1451. The mass map is produced using the distortions of the faint background galaxies as probes of the mass density of the cluster. The gray scale shown at the right edge of the map is in units of the critical density. The light map is the result of the smoothing of the magnitude of the clusters members belonging to the red sequence (see text for details).

by an angular radial coordinate θ and an azimuthal angle ϕ. For the SIS profile the convergence and the shear are given by

$$\kappa = \gamma = \frac{1}{2}\frac{\theta_{\rm E}}{\theta}, \tag{7}$$

where $\theta_{\rm E}$ is the Einstein radius, which is related to the one-dimensional velocity dispersion of the isothermal sphere ($\sigma_{\rm SIS}$) as

$$\theta_{\rm E} = 4\pi\frac{\sigma_{\rm SIS}^2}{c^2}\frac{D_{ls}}{D_s}. \tag{8}$$

The SIE profile (e.g., Kormann et al. 1994) has properties similar to those of SIS models, but the values of the shear and the convergence are now given by

$$\kappa = \gamma = \frac{1}{2}\frac{\theta_{\rm E}}{\theta} f\left[\cos(\phi-\alpha) + f^2\sin(\phi-\alpha)\right]^{-1/2}, \tag{9}$$

where $f < 1$ is the axial ratio b/a, α is the position angle of the ellipsoidal matter distribution, and ϕ is the azimuthal coordinate. For this model, in the weak-lensing regime ($\kappa \ll 1$), the shear is oriented tangentially to the direction to the center of mass.

The SIS model has only one free parameter, $\theta_{\rm E}$, whereas the SIE has three free parameters: $\theta_{\rm E}$, f, and α.

To check the isothermal assumption, we also fitted a power-law profile (PL), which is fully described by two parameters: the Einstein radius and a slope q. In this case we have

$$\kappa(\theta) = \frac{2-q}{2}\left(\frac{\theta}{\theta_{\rm E}}\right)^{-q} \tag{10}$$

and

$$\gamma(\theta) = \frac{q}{2}\left(\frac{\theta}{\theta_{\rm E}}\right)^{-q}. \tag{11}$$

In all cases the positions of the cluster center were defined in advance with the help of the mass maps. For each model, the best-fit parameters were obtained through minimization of the χ^2 statistic, defined as

$$\chi^2 = \sum_i \frac{(\epsilon_{t,i} - g_{t,i})^2}{\sigma_{\epsilon_t,i}^2 + \sigma_\epsilon^2}, \tag{12}$$

where $\epsilon_{t,i}$ and $\sigma_{\epsilon_t,i}$ are the tangential ellipticity and its error for the ith galaxy, $\sigma_\epsilon = 0.3$ (Mellier 1999) is the dispersion associated with galaxy intrinsic shapes, and $g_{t,i}$ is the tangential reduced shear at the position of this galaxy, which quantifies the ellipticity induced by the lensing distortion. For all models we consider here it may be assumed that, in the weak-lensing regime, $|g| = g_t$. This method of profile fitting is similar to the one developed by King & Schneider (2001) and has the advantage of avoiding data binning.

The center of mass was defined in general as the center of the mass map. When there is consistency between the peak of the mass map and a bright cluster galaxy (the dominant one in most cases), the latter one was used as the center position. In some cases (A2104, A3739, and A3888) the maximum of the mass map, and therefore the adopted center of mass, is in a position between bright cluster members, and in other cases (A85, A2811, and A1650) it is in a position uncorrelated with the cluster galaxies.

The best-fit parameters of SIS and SIE models are also shown in Table 2. We have estimated $\sigma_{\rm SIS}$ ($\sigma_{\rm SIE}$ for the elliptical model) from $\theta_{\rm E}$ using for each cluster an average value of D_{ls}/D_s obtained in a way analogous to that adopted by Dahle et al. (2002). Considering the minimum and average values of I magnitudes in our weak-lensing sample, we selected subsamples of HDF galaxies (Fernández-Soto et al. 1999), and from their photometric redshifts, the mean value of the distance ratio above was calculated. In this table we also show the average redshift of the galaxies used in the lensing analysis with their

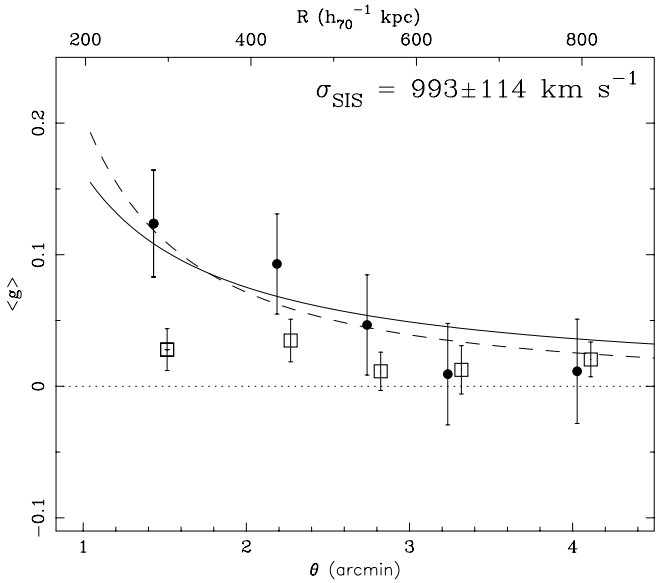

FIG. 4.—Shear profile for the cluster A1451. The filled symbols correspond to average ellipticies of the faint background galaxies projected tangentially to the cluster center. Each point represents nearly 1/5 of the galaxies. The open squares are the same, but for ellipticies projected in a direction 45° relative to the center. The solid and dashed lines show the best-fit SIS and power-law profiles, respectively.

respective uncertainties (which are not taken into account in the estimate of the uncertainties in σ_{SIS}).

Examples of the radial shear profile and the best-fit SIS and PIL profiles are shown in Figure 4.

A main drawback of the parametric approach is that many clusters may have irregular mass distributions, not properly described by the profiles adopted here. When fitting noisy data or clump mass distributions with the SIE profile, one often obtains unrealistic low values of the axial ratio ($f < 0.3$). Clusters for which this happened have an empty entry in Table 2. We dealt with it by adopting a constant value of $f = 0.3$ when the fit gives values smaller than this one. On the other hand, the value obtained for the position angle is quite robust, being rather insensitive to f. Soft-core (i.e., nonsingular) and Navarro et al. (1997) profiles have parameters, such as the core radius or the NFW concentration parameter, whose determination depends critically on information from the inner parts of the cluster. Since we do not have useful data in the central arcminute, or even at larger radius (which are important for NFW profiles), we are unable to properly fit our data using these models.

Another point that deserves mention in Table 2 are the small values of χ^2_{red}. This happens because of the large value of the intrinsic shape dispersion σ_ϵ.

4. DISCUSSION

4.1. *Mass and Light Distributions*

Although each galaxy cluster of our sample has particular features, as can be seen in the display of the mass and light distributions provided in the Appendix, there are some general trends and correlations that can be drawn from these maps. A detailed and more quantitative comparison of these distributions will be addressed in a future paper.

In most cases (17 out of 22), the center of mass of the cluster (nearly) coincides with the position of the brightest cluster galaxy (BCG) or the main galaxy clump. We are including in this category the clusters A22, A1437, and A2163, where the mass maps show peaks near the position of the central galaxy, despite the presence of more prominent peaks near the edges of the frame (see relevant figures in the Appendix).

Although most of the cluster mass maps show single clumps, an effect that can be attributed in part to poor resolution, some of them present secondary peaks (e.g., A1451 and A3695) or extensions of the main peak in the direction of substructures present in the light distribution (A2744, A2104, A2597, and A3739). Conversely, the clusters A1553 and A2163 present prominent light clumps without counterparts in the mass map.

For some clusters, the mass and light maps suggest the existence of "dark clumps" (mass concentrations without optical counterparts), but their reality is doubtful since most of them are near the edge of the observed cluster field. Nevertheless, in the map of A1451 (see Fig. 3) there is a significant structure south of the main cluster clump, with an extension to the west, that is not too close to the frame border and is not associated with bright cluster galaxies. Indeed, our bootstrapping of galaxy ellipticities shows that this is a robust feature. The X-ray isophotes of Valtchanov et al. (2002) do not show any emission excess at this region, either. The nature of this feature, whether it is a real dark clump belonging to A1451 or a background massive structure, will be the subject of future investigations. It is worth mentioning that, as a result of the filamentary structure in large scales, alignments of massive structures are not uncommon (e.g., Voit et al. 2001).

Dark matter profiles tend to present significant departures from circular symmetry. This can be noticed by the smaller values of χ^2_{red} presented by SIE in relation to the SIS fits, as well as by the uncertainties of σ_{SIE}, which are ~20% smaller for the noncircular profile. Furthermore, the mass maps often show elongated distributions, with major axis with position angles similar to those given by the SIE fitting. Sometimes the ellipticity inferred from the mass map is smaller than that from the SIE fitted profile. This is due to two reasons: first, the smoothing process in the mass map calculation tends to circularize features whose scales are smaller than the map resolution; second, as discussed before there is a bias toward small ellipticity values in the fitting of SIE profiles with noisy data.

A very robust result that comes from the SIE fits is that the major axis of the mass distribution is clearly aligned with the major axis of BCGs. This is shown in Figure 5, where we present the absolute value of the difference between the position angle of a BCG (from SExtractor) and the position angle given by the SIE mass model. For clusters without a clear dominant galaxy (A2744, A1451, A3888, and A3984), the direction linking the two first-ranked cluster members was adopted to characterize the orientation of the light distribution. On the other hand, for at least two cases (A1451 and A2426) the main direction of the dark matter distribution is more related with the direction linking bright cluster members than with the direction of the BCG.

The strong alignment between light and mass on megaparsec scales found here has also been detected, at smaller scales, by the excess of strong lensing features found in the direction of the major axis of BCGs (Luppino et al. 1999; L. Campusano et al. 2004, in preparation).

Considering that alignments between several cluster components (BCGs, cluster galaxies, substructures, and surrounding large-scale structures) have already been found (e.g., West et al. 1995; Plionis & Basilakos 2002), the present result reinforces the conclusion that clusters, in the same way as their dominant galaxies, have been formed by the anisotropic

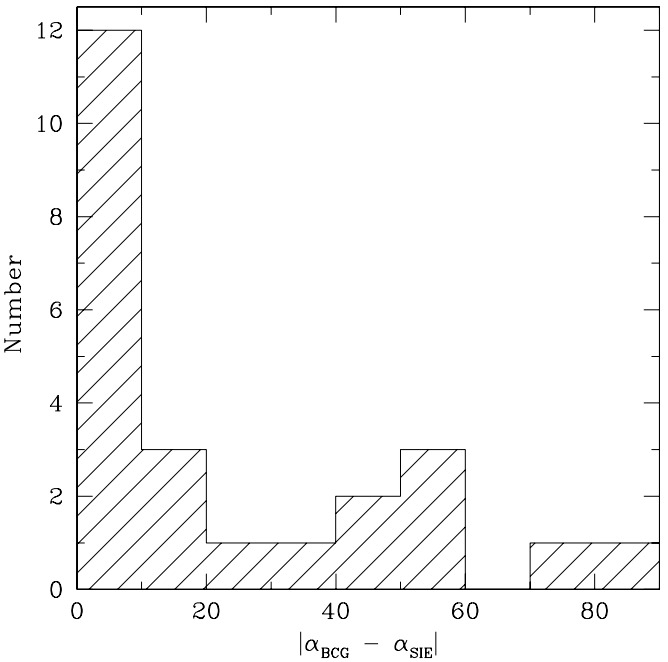

FIG. 5.—Alignment between the position angle of the brightest cluster galaxy α_{BCG} and that of the mass distribution α_{SIE}. For clusters without a clear dominant galaxy, the direction linking the two first ranked cluster members is used instead.

merger of smaller structures along large-scale filaments, in close agreement with numerous cosmological simulations based on the cold dark matter (CDM) paradigm (e.g., Jenkins et al. 1998).

It should be stressed here that the diffuse luminous halo associated with a cD galaxy tends to produce the opposite effect. This halo will produce a significant gradient in the background of a certain galaxy, which contaminates the measure of its shape, causing it to stretch in the radial direction. Since this halo is brighter in the direction of the major axis, galaxies located in this direction will be more affected. This is probably what is happening in A2029, which has a very luminous diffuse component (Uson et al. 1991) and where the major axis of the mass distribution is about 60° of the central cD major axis. The hypothesis of light contamination in this case is supported by the fact that when the central exclusion radius is increased from 60″ to 75″, it produces a major change in α, which becomes almost parallel to the BGC main axis, however without causing appreciable changes in σ_{SIE}. We did not detect such effect in any other cluster of the sample.

4.2. *The Dynamical State of Massive Clusters*

The dynamical state of the clusters in the present sample can be accessed through a comparison between the mass estimates made by weak-lensing, dynamical, and X-ray techniques. The key idea is that the weak-lensing signal is independent of the cluster dynamical state, whereas other techniques rely on assumptions of equilibrium.

We have collected measurements of T_X and σ_v from the literature (see Table 3). Assuming energy equipartition between cluster galaxies and gas, we may obtain an estimate of the temperature from our weak-lensing determination of σ_{SIS} (and for σ_{SIE}), through the relation (e.g., Sarazin 1988)

$$\sigma_{SIS}^2 = \frac{kT_{SIS}}{\mu m_H}, \quad (13)$$

where $\mu = 0.61$ is the mean molecular weight and m_H the hydrogen mass. The results are also in Table 3. In Figure 6 we present a comparison between temperatures computed in this way and those actually obtained with X-ray observations. In Figure 7 we compare the velocity dispersions determined through lensing with those obtained directly from galaxy velocities.

The first point to note in these figures is that for many clusters the weak-lensing results agree with X-ray or dynamical data within 1.5 σ. The clusters A1451, A1553, and A2163, however, show temperatures and velocity dispersions significantly in excess when compared with estimates derived from weak-lensing data, suggesting that they should be dynamically active. Actually, the analysis of the A2163 temperature map made by Markevitch & Vikhlinin (2001) with *Chandra* data shows at least two shocked regions and other evidence that the central region of this cluster is in a state of violent motion. In the same way, Valtchanov et al. (2002) describes A1451 as being in the final stage of establishing equilibrium after a merger event, whereas its high X-ray temperature (13.4 keV) would be probably due to a recent shock. A2744 seems to be an exception, since its temperature is significantly lower than the weak-lensing estimate. The nature of this cluster is discussed in more detail in § 4.4.

We present in Table 4 the weighted (by the error of the ratio) mean ratios $T_X/T_{SIS,SIE}$ and $(\sigma_v/\sigma_{SIS,SIE})^2$ for both SIS and SIE mass models, as well as their errors of the mean. These quantities are proportional to the ratio between the mass computed from the X-ray emission or cluster dynamics and the mass inferred from weak-lensing. For the clusters in our sample for which this analysis is possible, we verify that the temperature inferred from the lensing analysis is 17%–27% lower than that determined by X-ray observations; the squared velocity dispersions determined from galaxy velocities are also larger than that obtained from lensing, by a factor between 13% and 27%. These factors are smaller for the elliptical models. Other comparisons between dynamical and weak-lensing mass estimates have been made by Irgens et al. (2002) and Smail et al. (1997). Whereas the latter work has found values of σ_{SIS} roughly 50% greater than σ_v, the former has found a broad consistency between these two quantities.

Dividing the sample in clusters colder and hotter than $T_X = 8.0$ keV (or, equivalently, σ_v larger or smaller than 1122 km s^{-1}), the first set presents ratios consistent with unity within the errors, whereas the second set shows excess (relative to lensing results) of 40%–75%; see Table 4. Not surprisingly, all clusters that we have already identified as dynamically active belong to this second set.

Differences in temperature of the order of tenths of a percent are not unexpected, since some authors, using numerical simulations, claim that galaxies are 10%–20% "hotter" than the dark matter (Colín et al. 2000), whereas others find the opposite (e.g., Carlberg & Couchman 1989). However, differences as great as 50% should mean significant departures from relaxation.

These results find a natural explanation in the hierarchical scenario, where the most massive structures are being formed at this very moment. If this is the case, higher intracluster medium (ICM) temperatures are expected (compared to an equilibrium state), because the gas is heated by shocks produced by galaxy groups falling in to the cluster as well as mergers with other clusters (e.g., Markevitch et al. 2002).

Higher velocity dispersions are also expected, since the cluster dynamics will be affected by motion streams and substructures, that broaden the velocity distribution.

TABLE 3

Cluster Name (1)	$kT_{\rm SIS}$ (keV) (2)	$kT_{\rm SIE}$ (keV) (3)	$kT_{\rm X}$ (keV) (4)	References (5)	σ_v (km s^{-1}) (6)	N (7)	References (8)
A2744.....	$14.13^{+2.28}_{-2.11}$	$15.17^{+2.26}_{-2.10}$	$11.04^{+0.49}_{-0.45}$	1	1777^{+151}_{-125}	55	7
A22.....	$2.79^{+1.03}_{-0.87}$	$4.26^{+0.78}_{-0.73}$	...	...	98^{+126}_{-162}	...	8
A85.....	$5.34^{+1.04}_{-0.94}$	$5.45^{+1.00}_{-0.92}$	$6.51^{+0.16}_{-0.23}$	2	1097^{+76}_{-63}	305	9
A2811.....	$4.73^{+1.78}_{-1.49}$	$4.76^{+1.55}_{-1.33}$	$5.31^{+0.17}_{-0.16}$	3	695^{+200}_{-108}	13	10
A1437.....	$3.42^{+1.56}_{-1.27}$	$3.87^{+1.30}_{-1.11}$	...	...	...	...	...
A1451.....	$6.27^{+1.52}_{-1.36}$	$7.47^{+1.40}_{-1.28}$	$13.40^{+1.9}_{-1.5}$	4	1338^{+130}_{-90}	57	4
A1553.....	$5.42^{+2.40}_{-1.96}$	$5.37^{+2.00}_{-1.69}$	$9.16^{+1.02}_{-0.64}$	3	...	...	...
A1650.....	$4.88^{+1.60}_{-1.37}$	$7.25^{+1.54}_{-1.39}$	$5.68^{+0.30}_{-0.27}$	2	770	87	11
A1651.....	$0.28^{+2.90}_{-0.25}$	$1.85^{+1.61}_{-1.11}$	$6.22^{+0.45}_{-0.41}$	2	695^{+200}_{-108}	62	12
A1664.....	...	$1.58^{+1.29}_{-2.32}$	...	...	...	...	...
A2029.....	$6.86^{+0.87}_{-0.83}$	$7.03^{+0.87}_{-0.82}$	$7.93^{+0.39}_{-0.36}$	2	1164^{+98}_{-78}	93	12
A2104.....	$6.86^{+1.50}_{-1.35}$	$6.85^{+1.41}_{-1.28}$	$9.13^{+0.69}_{-0.45}$	3	1201 ± 200	51	13
A2163.....	$6.63^{+2.03}_{-1.76}$	$7.55^{+1.78}_{-1.60}$	$12.3^{+1.3}_{-1.1}$	5	1698	...	14
A2204.....	$6.72^{+1.49}_{-1.29}$	$6.81^{+1.41}_{-1.28}$	6.38 ± 0.23	2	...	...	...
A3695.....	$5.50^{+1.47}_{-1.30}$	$6.17^{+1.38}_{-1.24}$	$6.67^{+2.84}_{-1.99}$	2	779^{+67}_{-49}	96	12
A3739.....	$9.20^{+1.79}_{-1.63}$	$9.41^{+1.51}_{-1.40}$	...	...	...	...	...
A2345.....	$5.25^{+1.72}_{-1.47}$	$5.93^{+1.62}_{-1.42}$	...	...	...	...	...
A2384.....	$3.45^{+1.28}_{-1.08}$	$4.02^{+1.11}_{-0.97}$	...	...	...	...	...
A2426.....	$2.90^{+1.52}_{-1.20}$	$3.85^{+1.36}_{-1.15}$	...	...	990	23	11
A3856.....	$6.37^{+1.34}_{-1.21}$	$6.74^{+1.24}_{-1.14}$	...	...	729 ± 142	22	14
A3888.....	$6.12^{+1.66}_{-1.46}$	$6.46^{+1.70}_{-1.50}$	$8.46^{+3.6}_{-2.53}$	2	1102^{+137}_{-107}	50	7
A3984.....	$7.59^{+1.11}_{-1.03}$	$8.30^{+1.02}_{-0.96}$	...	...	...	...	...
A2597.....	$3.83^{+1.06}_{-0.93}$	$4.56^{+0.82}_{-0.75}$	$4.40^{+0.4}_{-0.7}$	6	597^{+117}_{-90}	29	8
A4010.....	$3.17^{+1.00}_{-0.87}$	$3.88^{+0.81}_{-0.74}$	...	...	625^{+127}_{-95}	36	12

NOTES.—Col. (1) Cluster name. Cols. (2) and (3): X-ray temperatures inferred from the SIS/SIE modeling of the shear data. Col. (4): X-ray temperature with 66% uncertainties from the literature. Col. (5): References for $T_{\rm X}$. Col. (6): Velocity dispersions found in the literature. Col. (7): Number of galaxies used to determine σ_v. Col. (8): References for σ_v.

REFERENCES.—(1) Allen 2000; (2) Ikebe et al. 2002; (3) White 2000; (4) Valtchanov et al. 2002; (5) Markevitch & Vikhlinin 2001; (6) Markevitch et al. 1998; (7) Girardi & Mezzeti 2001; (8) De Propris et al. 2002; (9) Durret et al. 1998; (10) Collins et al. 1995; (11) Andernach & Tago 1998; (12) Fadda et al. 1996; (13) Liang et al. 2000; (14) Squires et al. 1997.

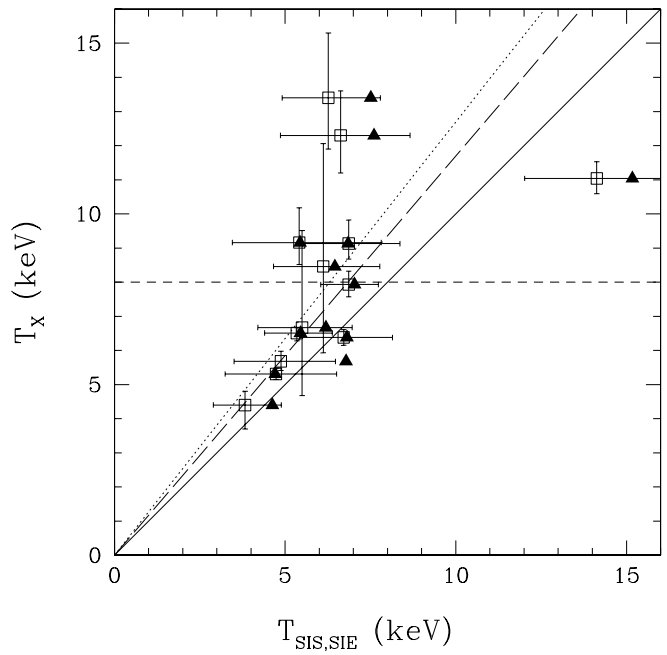

FIG. 6.—Comparison between the ICM temperatures inferred by the fitting of isothermal profiles to the shear data, $T_{\rm SIS}$ and $T_{\rm SIE}$, and from X-ray measurements, $T_{\rm X}$. The squares correspond to the spherical model and triangles to the elliptical. The error bars of the latter were suppressed for clarity. The solid line is defined by $T_{\rm SIS,SIE} = T_{\rm X}$. The dotted and long-dashed lines show the best obtained by the SIS and SIE models, respectively, when the origin is kept constant. The short-dashed line indicate $T_{\rm X} = 8$ keV. Clusters with higher temperatures show signals of dynamic activity.

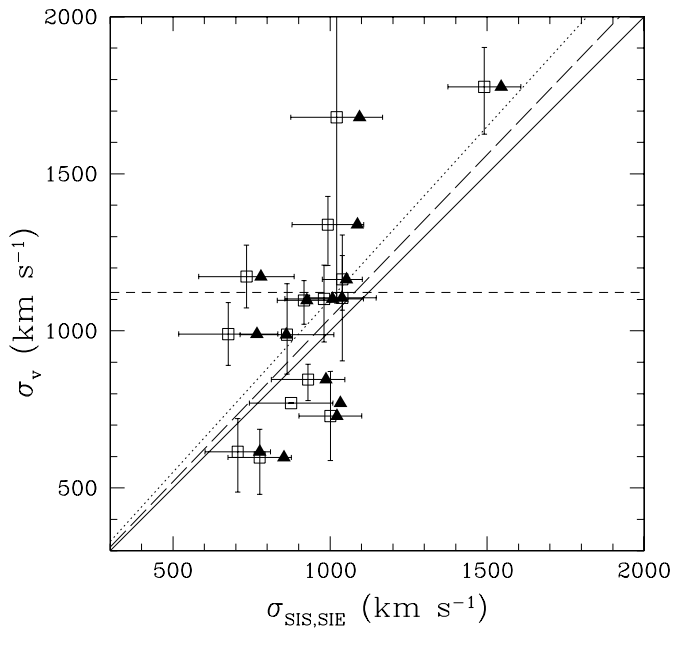

FIG. 7.—Comparison between the velocity dispersion found by fitting isothermal profiles to the shear data, $\sigma_{\rm SIE,SIE}$, and those estimated through spectroscopic measurements, σ_v. The squares correspond to the spherical model and triangles to the elliptical. The error bars of the latter were suppressed for clarity. The solid line is defined by $\sigma_{\rm SIS,SIE} = \sigma_v$. The dotted and long-dashed lines show the best fit obtained by the SIS and SIE models, respectively, when the origin is kept constant. The short-dashed line indicate $\sigma_v = 1122$ km s^{-1}, which correspond to gas temperatures of $T_{\rm X} = 8$ keV. Clusters with higher velocity dispersions show signals of dynamic activity.

TABLE 4

WEIGHTED MEANS AND ERRORS OF THE RATIO BETWEEN CLUSTER TEMPERATURES (X-RAY AND DYNAMICAL) AND WEAK LENSING–INFERRED VALUES

Parameter (1)	All (2)	$T_X < 8.0$ keV $\sigma_v < 1122$ km s^{-1} (3)	$T_X > 8.0$ keV $\sigma_v > 1122$ km s^{-1} (4)
T_X/T_{SIS}	1.27 ± 0.09	1.14 ± 0.03	1.55 ± 0.19
T_X/T_{SIE}	1.17 ± 0.08	1.04 ± 0.05	1.42 ± 0.15
$(\sigma_v/\sigma_{SIS})^2$	1.27 ± 0.15	1.06 ± 0.15	1.76 ± 0.15
$(\sigma_v/\sigma_{SIE})^2$	1.13 ± 0.14	0.93 ± 0.14	1.60 ± 0.22

It is worth investigating further whether $T_X \sim 8$ keV may indeed be considered a threshold to discriminate between relaxed and active clusters, because many studies of the cluster mass function are based on X-ray data, which usually select the most massive clusters. For example, 11 out of the 106 cluster of the sample selected by Reiprich & Böhringer (2002) have temperatures equal to or higher than 8 keV. It is also interesting to note that if we use an empirical σ-T relation for clusters like the one of Xue & Wu (2000), we find a slightly better agreement between lensing and X-ray properties; the main trends discussed before, however, remain the same.

4.3. *Comparison of σ_{SIS} with Previous Estimates*

Some of the clusters studied here already have a weak-lensing analysis made by other authors. Table 5 compares our σ_{SIS} with other works that used the same model.

4.3.1. *A2744*

The largest difference between the results in Table 5 is for A2744. It has a very flat shear profile (see Fig. 8). Smail et al. (1997) found for this cluster $g \sim 0.2$ inside a radius of $1'$, whereas our data give $g \sim 0.14$ in $1.'0 < R < 3.'2$. Taking into account that the Smail et al. (1997) analysis used galaxies fainter than those considered here, thus probably more distant, and also closer to the cluster center, their detection of higher gravitational distortions is not unexpected. Indeed, as discussed in § 4.4, this cluster probably correspond to two structures close to the line of sight. Isothermal laws are inadequate, and the fact that the χ^2_{red} found for this cluster is the highest in this sample confirms it.

4.3.2. *A2104, A2204, and A2345*

There are three clusters studied by Dahle et al. (2002) in common with the present sample: A2104, A2204, and A2345. For the last two, the values of σ_{SIS} obtained by these authors are consistent with the values presented here, but for A2104 there is a large difference. A point that is worth mentioning is that these authors used the approximation $g \sim \gamma$ instead of $g = \gamma/(1 - \kappa)$. Adopting the same approximation to fit our data with the SIS profile, we obtain the following values: 1092, 1086, and 957 km s^{-1}, respectively, instead of 1039, 1028, and 909 km s^{-1}. It demonstrates that this approximation causes an overestimation of the inferred velocity dispersion by a factor of ~5%, depending on the cluster density and the field size, but this is not the cause of this difference. In fact, Dahle et al. (2002) report problems with their images of A2104. For their weak-lensing analysis they used only one I-band image, obtained with 1 hr integration with a seeing (FWHM) of $0.''7$ at the University of Hawaii 2.24 m telescope. Our data for A2104, on the other hand, have been collected in one of the best nights at VLT in that semester, when the seeing was $0.''41$. This makes us very confident of our results.

TABLE 5

COMPARISON OF σ_{SIS} WITH OTHER WORKS

Cluster Name (1)	σ_{SIS} (km s^{-1}) Present work (2)	σ_{SIS} (km s^{-1}) Others' work (3)	References (4)
A2744	1491 ± 116	870^{+41}_{-95}	1
A2104	1039 ± 108	1390 ± 180	2
A2163	1021 ± 146	740	3
A2204	1028 ± 104	950^{+210}_{-250}	2
A2204	1028 ± 104	1035^{+65}_{-71}	4
A2345	909 ± 138	870^{+260}_{-320}	2

NOTES.—Col. (1): Cluster name. Col. (2): Value of σ_{SIS} from this work. Col. (3): Value of σ_{SIS} from the literature. Col. (4): Reference of the other weak-lensing measurement.

REFERENCES.—(1) Smail et al. 1997; (2) Dahle et al. 2002; (3) Squires et al. 1997; (4) Clowe & Schneider 2002.

Our A2104 mass map is also very different from the one obtained by these authors. Accordingly to them, the mass distribution is nearly perpendicular to the major axis of the central D galaxy, which is also along the direction of the two brightest galaxies, and is the direction where the gravitational arcs are seen. However, our mass map as well as the fitting of SIE models show that A2104 has an elliptical mass distribution aligned with the central galaxy major axis, as expected if the BCG light is a good tracer of the cluster potential (see, e.g., Mellier et al. 1993).

4.3.3. *A2163*

Our estimate of the velocity dispersion of A2163 is also much higher than that reported by Squires et al. (1997). These authors have observed this cluster in V and I with total exposures of 1 hr at the 3.6 m CFHT, under seeing of $\sim 0.''8$. They have used ~700 galaxies fainter than $I = 20.5$ mag or $V = 22.0$ mag for the lensing analysis, in a field of 7×7 arcmin.

Here we have used a much smaller sample of background galaxies, in a field of comparable size, because we have considered only galaxies fainter than $R = 23.3$ mag, which is roughly 2.0 mag fainter than the bright end limit used by Squires et al. (1997). The images of this cluster were taken on the same night as those of A2104, when the seeing was exceptional. A2163 is at a moderately high redshift ($z = 0.2$) and lies in a region of the sky not too far from the Galactic plane ($b = 30.^\circ5$), where the star field is dense and the Galactic absorption is not negligible ($A_V = 1.74$; Schlegel et al. 1998), so the weak-lensing sample of Squires et al. (1997) may be more affected by contamination by stars and foreground and cluster galaxies than the present one. This might be the cause of a possible dilution of the lensing signal measured by them. Indeed, adopting a comparable magnitude cutoff, $R > 21.5$ mag, we obtain $\sigma_{SIS} = 887 \pm 145$ km s^{-1}, which is much closer to the Squires et al. (1997) result.

4.3.4. *A2204*

Table 5 shows that our results for A2204 are in very close agreement with those from Clowe & Schneider (2002). This work is based on images taken with the wide-field camera of the ESO/MPI 2.2 m telescope ($34' \times 34'$), indicating that when the data are well described by an isothermal mass profile, as

is the case of A2204, the small field of the FORS1 camera does not introduce relevant systematic errors.

4.4. *The Peculiar Case of A2744*

This cluster, also known as AC 118, is interesting for several reasons. It is the most distant ($z = 0.308$) and apparently the most massive cluster in our sample. It is also the only cluster where we have found gravitational radial arcs (see L. Campusano et al. 2004, in preparation) and has a flat shear profile that is very poorly fitted by isothermal models. Furthermore, its weak-lensing mass is smaller than the virial mass but, surprisingly, significantly larger than that from the X-ray estimate. We should bear in mind that the use of an isothermal profile to fit a shallow mass distribution tends to underestimate the cluster mass, since the shear depends more on the density gradient than on the density actual value. But an important clue for the interpretation of this cluster comes from the dynamical analysis of Girardi & Mezzeti (2001), who found a velocity distribution with two superposed peaks, produced by two structures along the line of sight, with velocity dispersions of 1121 and 682 km s^{-1}. Weak lensing, in this case, is sensitive to the total mass, but single isothermal mass models are clearly inadequate for this system. On the other side, the mass inferred from the X-ray analysis will be dominated by the luminous and hotter structure; for $\sigma_v = 1121$ km s^{-1} a value of $T_X = 8.0$ keV is expected, somewhat smaller than the X-ray measurement (see Table 3). In this scenario the X-ray luminosity is the sum of the luminosities of both structures. The value of L_X for A2744 is actually very high (22.05×10^{44} ergs s^{-1}), ranked in second place in this sample. Of course, both T_X and L_X may be increased with respect to their equilibrium values by shocks between these two substructures and, therefore, all these results are consistent with the hypothesis that A2744 is actually two close structures along the line of sight or even a pair of clusters in process of merging.

4.5. *The Slope of the Mass Profile*

The slope q of the power-law fit of the projected mass distribution spans a large range, from almost flat ($q = 0.02$) to very steep ($q = 2.0$). The general trend, however, is that the profiles tend to be flatter than what is expected in the isothermal case ($q = 1$).

This is not a surprise, since in the central regions we are sampling most of the numerical simulations predict density profiles flatter than isothermal (Navarro et al. 1997; Ghigna et al. 2000). On the other side, contamination by cluster galaxies, which tend to decrease the shear signal in the central regions, and substructures, which increase the signal of the outer regions, is probably enhancing this flatness. If the actual mass density profile is really flatter than the isothermal, the SIS fit will underestimate the mass estimate by an amount that depends on the actual shape of the dark matter radial profile.

Although we are postponing a detailed discussion on the morphology of the mass and light distribution to another paper, deeper and wider observations are necessary to confirm or reject the tendencies found in the parametric fits of our data set.

4.6. *Negative Weak-Lensing Detections: A1651 and A1664*

For only two out of 24 clusters (8.3%) we were unable to reconstruct the two-dimensional mass distribution. This number is comparable to that obtained by Dahle et al. (2002), who failed to detect weak-lensing in one cluster out of 39 (2.5%). These authors have adopted a sample threshold of $L_X = 10^{45}$ ergs s^{-1}, 2 times larger than ours. Our two failure cases are clusters with luminosities below this threshold.

For A1664 we were unable to reconstruct the mass density distribution and to fit an SIS profile, and we have a very marginal detection when fitting an SIE profile. This cluster is at $z = 0.13$ and has an X-ray luminosity very close to our threshold. Neither the X-ray temperature nor the velocity dispersion is available in literature for this object. Moreover, only 246 galaxies were used for the weak-lensing analysis (the third-smallest number of the sample). It seems that we were unable to detect the weak shear because its signal is small and is dominated by the noise in its distortion map.

The case of A1651 is less clear, since this cluster seems to be more massive than A1664 (see Table 3). In fact, the SIS fit resulted in a very small value for σ_{SIS}, but the SIE fit led to a significant detection, resulting in a value of $\sigma_{SIS} = 539 \pm 198$ km s^{-1}, consistent with the dynamical velocity dispersion found in literature, 695^{+200}_{-108} km s^{-1} (Fadda et al. 1996). The position angle of the SIE model is almost coincident with that of the BCG major axis, as found for most of the clusters in our sample. However, the lensing signal is still too low to allow a successful mass reconstruction by LENSENT.

Another common factor for these two cases is that seeing conditions during the observations were within the worst quartile of the sample. This puts in evidence how critical seeing conditions are for ground-based weak-lensing studies.

5. CONCLUSIONS

We analyzed the mass content of galaxy clusters belonging to a well-defined sample of 24 Abell clusters brighter than $L_X = 5 \times 10^{44}$ ergs s^{-1} (0.1–2.4 keV; Ebeling et al. 1996), spanning over the redshift range 0.05–0.31, using current techniques of weak-lensing analysis and homogeneous observing material of subarcsecond image quality. The resulting catalog of mass maps determined for 22 of these clusters, together with the corresponding light maps, has been put together in the Appendix. Our main conclusions may be summarized as follows:

1. We were able to detect significant weak-lensing signal in 22 out of 24 clusters. This high success rate shows the feasibility of weak-lensing studies with 8 m class telescopes using service mode observations and relatively short exposure times. It also indicates that the X-ray luminosity is indeed a good way to select massive clusters. Nondetections in A1651 and A1664 are probably due to a combination of poorer observing conditions and low mass content.
2. The center of the mass and light distributions of the clusters are coincident for $\sim$77% of the sample (17 out of 22).
3. Few clusters present massive substructures, which can be due, in part, to small fields (0.4–1.8 Mpc on a side) and the relatively low resolution of the mass maps. When significant substructures are seen, they are generally associated with bright cluster members. However, in at least one cluster (A1451) there seems to be a substructure without a clear optical counterpart.
4. The clusters analyzed here present important departures from spherical symmetry, as can be verified by the better fits obtained with elliptical profiles. This result confirms the nonsphericity of dark matter halos found in cosmological simulations (e.g., Jing & Suto 2002).
5. We have found, for the first time in a statistically significant sample, that the dark matter and brightest cluster galaxy major axes are strongly aligned: for 62.5% of the clusters (15 out of 24) the difference between their position angles is smaller than 20°.

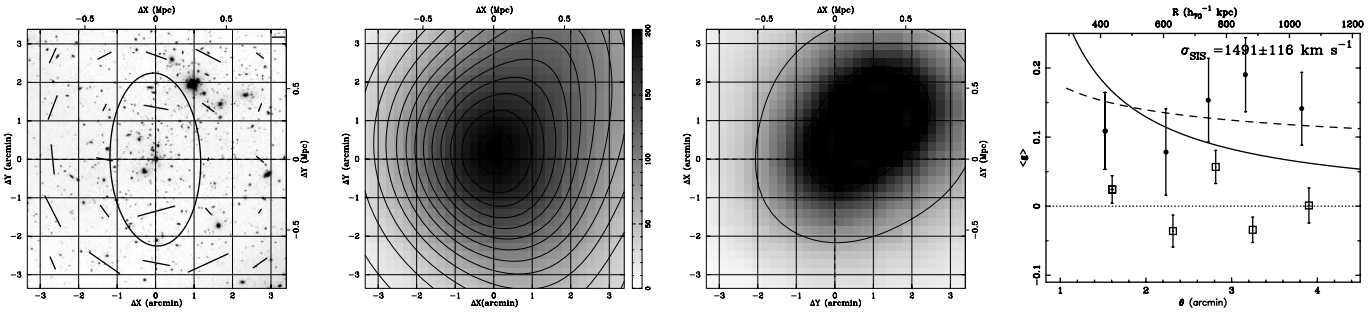

FIG. 8.—Results of the weak-lensing analysis of A2744. *Left*: Cluster image. *Left center*: Mass map, i.e., the surface density distribution reconstructed from the shear data. *Right center*: Distribution of light coming from cluster members that belong to the cluster red sequence. *Right*: Radial shear profile. See Appendix for complete description. [*See the electronic edition of the Journal for additional figures in this series*.]

6. Most clusters are in or near a state of dynamical equilibrium. This diagnosis derives from the agreement between their velocity dispersions and the temperature of their ICM, directly measured and/or inferred from weak-lensing data. Except for A2744, A1451, and A2163, which also present evidence of substructures or other complexities, the other clusters show agreement between these quantities at a 1.5 σ level.

7. Clusters in our sample with $T_X > 8$ keV (or $\sigma_v > 1120$ km s^{-1}) show signs of dynamical activity. A2163 and A1451 present large differences between lensing and dynamical mass estimates and seem to be far from equilibrium. In both cases, this conclusion corroborates previous X-ray analysis.

8. A2744 is the single cluster in this sample that has an X-ray–measured temperature more than 1 σ below the value inferred by weak-lensing. Taking also into account the complex dynamics of this cluster, we can explain this discrepancy by assuming that A2744 is a superposition of two clusters along the line of sight, near each other or in process of merging.

Most of these conclusions support a hierarchical scenario in which massive bodies are formed by the agglomeration of smaller ones, and the departures from equilibrium described above are indeed evidence that some clusters that are at the top of the mass function are still in the process of active evolution.

This work is based on observations collected at the European Southern Observatory, Chile (ESO P67.A-0597). E. S. C. and L. S. acknowledge support by Brazilian agencies FAPESP (processes 02/07337-6 and 01/0742-7), CNPq, and PRONEX, and E. S. C. is grateful to the Latin American Astronomy Network/UNESCO for funding travel to Chile. J. P. K. acknowledges support from CNRS and Caltech. E. S. C. also thanks the hospitality of the Department of Astronomy of the University of Chile and of the Laboratoire d'Astrophysique of the Observatoire Midi-Pyrénées. We are also grateful to Gastão Lima Neto and Ronaldo de Souza for useful discussions and Sarah Bridle and Phil Marshall for making their software, IM2SHAPE and LENSENT, available to us. We acknowledge Heinz Andernach for giving us access to an updated version of the compilation of Abell cluster redshifts by Andernach & Tago (1998).

APPENDIX

MASS AND LIGHT MAPS

In this Appendix we present figures referent to the weak-lensing analysis (Fig. 8). In each figure there are four panels. In the first panel (*from left to right*) we show the cluster image with superimposed sticks that represent the average ellipticities and position angles of the background galaxies. The size of the stick is proportional to the ellipticity. The scale bar in the top right corner of this panel represents an ellipticity of 0.1. We also present an ellipse with the axial ratio and position angle of the best-fit SIE profile. In the second panel, we show the mass maps, that is, the surface density distribution reconstructed from the shear data, in units of the critical surface density. The contours are in intervals of $1.5 \times 10^{12}\ M_\odot$ Mpc^{-2}. The third panel shows the distribution of light coming from cluster members that belong to the cluster red sequence, in arbitrary units, smoothed with a Gaussian similar to the one used to produce the mass map. The contours are in intervals of $1 \times 10^{11}\ L_\odot$ Mpc^{-2} in the V band. The fourth panel presents the radial shear profile, where the filled circles represent the average ellipticities projected tangentially to the direction to the cluster center, and the open squares show the ellipticities project in a direction 45° from the tangential one. The solid line represents the best-fit SIS profile and the dashed line the power-law profile.

REFERENCES

Allen, S. W. 2000, MNRAS, 315, 269
Allen, S. W., Schmidt, R. W., & Fabian, A. C. 2002, MNRAS, 334, 11
Andernach, H., & Tago, E. 1998, in Proc. Large-Scale Structure: Tracks and Traces, ed. V. Müller, S. Gottlöber, J. P. Mücket, & J. Wambsganss (Singapore: World Scientific), 147.
Athreya, R. M., Mellier, Y., van Waerbeke, L., Pelló, R., Fort, B., & Dantel-Fort, M. 2002, A&A, 384, 743
Bahcall, N. A., Fan, X. 1998, ApJ, 504, 1
Bahcall, N. A., Lubin, L. M., & Dorman, V. 1995, ApJ, 447, L81
Bardeau, S., Kneib, J.-P., Czoske, O., Soucail, G., Smail, I., & Ebeling, H. 2004, A&A, submitted (astro-ph/0407255)
Bertin, E., & Arnouts, S. 1996, A&AS, 117, 393
Bridle, S. 2002, in The Shapes of Galaxies and their Dark Halos, ed. P. Natarajan (Singapore: World Scientific), 38
Bridle, S. L., Hobson, M. P., Lasenby, A. N., & Saunders, R. 1998, MNRAS, 299, 895

Carlberg, R. G., & Couchman, H. M. P. 1989, ApJ, 340, 47
Carlberg, R. G., Yee, H. K. C., Ellingson, E., Abraham, R., Gravel, P., Morris, S., & Pritchet, C. J. 1996, ApJ, 462, 32
Clowe, D., & Schneider, P. 2002, A&A, 395, 385
Colín, P., Klypin, A. A., & Kravtsov, A. V. 2000, ApJ, 539, 561
Collins, C. A., Guzzo, L., Nichol, R. C., & Lumsden, S. L. 1995, MNRAS, 274, 1071
Dahle, H., Kaiser, N., Irgens, R. J., Lilje, P. B., & Maddox, S. J. 2002, ApJS, 139, 313
De Propris, R., et al. 2002, MNRAS, 329, 87
Durret, F., Felenbork, P., Lobo, C., & Slezak, E. 1998, A&AS, 129, 281
Ebeling, H., Voges, W., Böhringer, H., Edge, A. C., Huchra, J. P., & Briel, U. G. 1996, MNRAS, 281, 799
Fadda, D., Girardi, M., Giuricin, G., Mardirossian, F., & Mezzetti, M. 1996, ApJ, 473, 670
Fernández-Soto, A., Lanzetta, K. M., & Yahil, A. 1999, ApJ, 513, 34
Fort, B., & Mellier, Y. 1994, Astron. Astrophys. Rev., 5, 239
Geller, M. J., & Beers, T. C. 1982, PASP, 94, 421
Ghigna, S., Moore, B., Governato, F., Lake, G., Quinn, T., & Stadel, J. 2000, ApJ, 544, 616
Girardi, M., & Mezzeti, M. 2001, ApJ, 548, 79
Goto, T., et al. 2002, PASJ, 54, 515
Henry, J. P., & Arnaud, K. A. 1991, ApJ, 372, 410
Hoekstra, H., Franx, M., Kuijken, K., & van Dokkum, P. G. 2002, MNRAS, 333, 911
Ikebe, Y., Reiprich, T. H., Böhringer, H., Tanaka, Y., & Kitayama, T. 2002, A&A, 383, 773
Irgens, R. J., Lilje, P. B., Dahle, H., & Maddox, S. J. 2002, ApJ, 579, 227
Jenkins, A., et al. (The Virgo Consortium). 1998, ApJ, 499, 20
Jing, Y. P., & Suto, Y. 2002, ApJ, 574, 538
Kauffmann, G., Colberg, J. M., Diaferio, A., & White, S. D. M. 1999, MNRAS, 303, 188
King, L. J., & Schneider, P. 2001, A&A, 369, 1
Kneib, J.-P., Ellis, R. S., Smail, I., Couch, W. J., & Sharples, R. M. 1996, ApJ, 471, 643
Kormann, R., Schneider, P., & Bartelmann, M. 1994, A&A, 284, 285
Kuijken, K. 1999, A&A, 352, 355
Lacey, C., & Cole, S. 1994, MNRAS, 271, 676
Liang, H., Lémonon, L., Valtchanov, I., Pierre, M., & Soucail, G. 2000, A&A, 363, 440
Luppino, G. A., Gioia, I. M., Hammer, F., Le Fèvre, O., & Annis, J. A. 1999, A&AS, 136, 117
Markevitch, M., Forman, W. R., Sarazin, C. L., & Vikhlinin, A. 1998, ApJ, 503, 77
Markevitch, M., Gonzalez, A. H., David, L., Vikhlinin, A., Murray, S., Forman, W., Jones, C., & Tucker, W. 2002, ApJ, 567, L27
Markevitch, M., & Vikhlinin, A. 2001, ApJ, 563, 95
Marshall, P. J., Hobson, M. P., Gull, S. F., & Bridle, S. L. 2002, MNRAS, 335, 1037
Mellier, Y. 1999, ARA&A, 37, 127
Mellier, Y., Fort, B., & Kneib, J.-P. 1993, ApJ, 407, 33
Navarro, J. F., Frenk, C. S., & White, S. D. M. 1997, ApJ, 490, 493
Plionis, M., & Basilakos, S. 2002, MNRAS, 329, L47
Press, W. H., & Schechter, P. 1974, ApJ, 187, 425
Reiprich, T. H., & Böhringer, H. 2002, ApJ, 567, 716
Sarazin, C. L. 1988, X-Ray Emission from Clusters of Galaxies (Cambridge: Cambridge Univ. Press)
Schlegel, S., Finkbeiner, D. P., & Davis, M. 1998, ApJ, 500, 525
Smail, I., Ellis, R. S., Dressler, A., Couch, W. J., Oemler, A., Sharples, R. M., & Butcher, H. 1997, ApJ, 479, 70
Smith, G. P., Edge, A. C., Eke, V. R., Nichol, R. C., Smail, I., & Kneib, J.-P. 2003, ApJ, 590, L79
Sodré, L., Jr., Capelato, H. V., Steiner, J. E., & Mazure, A. 1989, AJ, 97, 1279
Sodré, L., Jr., Proust, D., Capelato, H. V., Lima Neto, G. B., Cuevas, H., Quintana, H., & Fouqué, P. 2001, A&A, 377, 428
Squires, G., Neumann, D. M., Kaiser, N., Arnaud, M., Babul, A., & Böhringer, H. 1997, ApJ, 482, 648
Tyson J. A., Valdes, F., & Wenk, R. A. 1990, ApJ, 349, L1
Uson, J. M., Bough, S. P., & Kuhn, J. R. 1991, ApJ, 369, 46
Valtchanov, I., Murphy, T., Pierre, M., Hunstead, R., & Lémonon, L. 2002, A&A, 392, 795
Voit, G. M., Evrard, A. E., & Bryan, G. L. 2001, ApJ, 548, L123
West, M. J., Jones, C., & Forman, W. 1995, ApJ, 451, L5
White, D. A. 2000, MNRAS, 312, 663
White, S. D. M., & Frenk, C. S. 1991, ApJ, 379, 52
Xue, Y.-J., & Wu, X.-P. 2000, ApJ, 538, 65